Study of Ionosphere Irregularities over the Iberian Peninsula during Two Moderate Geomagnetic Storms Using GNSS and Ionosonde Observations

Saioa A. Campuzano [1,*] , Fernando Delgado-Gómez [1], Yenca Migoya-Orué [2], Gracia Rodríguez-Caderot [1], Miguel Herraiz-Sarachaga [1,3] and Sandro M. Radicella [1,4]

[1] Department of Physics of the Earth and Astrophysics, Faculty of Physics, Complutense University of Madrid, Pl. Ciencias 1, 28040 Madrid, Spain
[2] The Abdus Salam International Centre for Theoretical Physics (ICTP), 34151 Trieste, Italy
[3] Instituto de Matemática Interdisciplinar (IMI), 28040 Madrid, Spain
[4] Institute for Scientific Research, Boston College, Chestnut Hill, MA 02467, USA
[*] Correspondence: sacampuzano@ucm.es

Abstract: Studies on the irregularities of the ionosphere during disturbed geomagnetic conditions are fundamental to understanding the complex dynamics taking place in the upper atmosphere. In this work, different data sources are used to study the ionosphere effects of two moderate geomagnetic storms, 26–27 February 2014 and 17–18 September 2021, over the Iberian Peninsula. Data are obtained from digital ionosondes in Spain, Italy and Greece; the Global Navigation Satellite System (GNSS) derived Total Electron Content (TEC) and Rate Of TEC Index (ROTI) from several receiver stations in Spain, Portugal and Morocco; and the UPC Quarter-of-an-hour time resolution Rapid GIM (UQRG), vertical TEC global ionosphere maps (GIMs), produced at 15 min intervals by the Universitat Politecnica de Catalunya (UPC, Spain). This analysis showed that, during the two moderate storms, spread-F and high values of ROTI, indicating the presence of irregularities, are found in a very localized area (Southern Iberian Peninsula and northwest Africa) and local times (night-time). However, no irregularities are found eastwards and northwards of the location indicated. We propose some possible explanations for these observations for both the storms, one of them related to the position of the Equatorial Ionosphere Anomaly (EIA) and the other one attributed to the Perkins' instabilities.

Keywords: ionosphere; geomagnetic storms; digital ionosonde; TEC; GIM

1. Introduction

It is well known that ionosphere F-region irregularities originate at night near the geomagnetic equator, rise in altitude, and, following the magnetic lines of force at high altitudes, reach latitudes far away from the equator. The scale size of these irregularities ranges from centimetres to kilometres [1]. In particular, after sunset, these plasma irregularities can be seen as spread-F in ionograms [2]. A detailed description of spread-F occurrence and behaviour in latitude has been given recently by Lan et al. [3] (and references therein) by using data from Chinese ionosonde stations. Alfonsi et al. [4], using data from a digital ionosonde at low latitude in South America, discuss the role of travelling ionospheric disturbances in the causation of irregularities, seen as spread-F. These irregularities are also seen as plasma bubbles in radar maps [5]. Other phenomena, such as airglow [6], high values of Total Electron Content (TEC) rate of change (ROT), and its associated scintillation of radio wave signals (e.g., [7,8]), can also be observed. From the ROT, an index, ROTI (TEC rate of change index), was introduced as a measure of ionosphere irregularities from the Global Navigation Satellite System (GNSS)-derived TEC values by Pi et al. [9]. The occurrence characteristics of high values of ROTI at low latitudes in Africa have been

discussed by Abe et al. [10], by finding the longitudinal differences of such occurrences. On the other hand, Thanh et al. [11] have analysed the behaviour of ROTI over low latitudes in Southeast Asia, in order to characterize ionosphere irregularities.

Low-latitude ionosphere is characterized by the presence of the Equatorial Ionosphere Anomaly (EIA), and ionosphere irregularities are linked to the development of the EIA. The EIA ([12] and references therein) is formed mainly from the uplift of plasma near the equator, by upward E×B drift, and its diffusion north and south along magnetic field lines. This process creates an electron density minimum near the magnetic equator and crests at $\pm$ 15° geomagnetic latitudes. A stronger EIA arises during geomagnetic storms via the simultaneous impulsive action of an eastward prompt penetration electric field and an equatorward neutral wind. Under these conditions, the electron density of the crests increases and moves to higher latitudes (see e.g., [13–15]). Simulations performed by Lin et al. [16] showed the poleward expansion of the EIA peaks and the ratio of the TEC increase between storm and pre-storm conditions; this combined the Sheffield University Plasmasphere-Ionosphere Model (SUPIM), used for electron densities, with the National Center for Atmospheric Research (NCAR) Thermosphere Ionosphere General Circulation Model (TIEGCM) when E×B drift plus equatorward winds are considered.

Cherniak and Zakharenkova [17] and Kashcheyev et al. [18], using GNSS receivers-derived TEC, and Swarm and DMSP satellites on board measurements, found for the first time that during the severe geomagnetic storm (as defined in terms of the Dst geomagnetic index) of 22–23 June 2015, large irregularities were observed in Southern Europe (Spain, Portugal, Southern France and Italy). The latter work shows that the occurrence of irregularities during that storm, observed as high values of ROTI, are located in the western longitude of the African–European sector but not in the eastern longitude of the same sector. The observation of such phenomena in middle geomagnetic latitudes could be related to the poleward displacement of the EIA from lower latitudes during geomagnetic storms. Azzouzi et al. [19] analysed the ionosphere effects of the large solar and the geomagnetic events of October 2013 in the Europe–African sector. They did not observe evidence of the relevant effects on Southern Europe.

The main goal of our work was to analyse the ionosphere response to two moderate geomagnetic storms over the Iberian Peninsula, particularly in the southern sector, and check whether the northern displacement of the EIA suggested by previous authors during more intense geomagnetic storms is also observed in moderate ones. The two geomagnetic storms under investigation occurred on 26–27 February 2014 and 17–18 September 2021. They were selected because (1) both occurred at the same local time, i.e., during the night of the European sector, (2) both were moderate and displayed a similar behaviour in the Dst, with the minimum of the Dst being higher in the case of the 2014 storm, and (3) in a preliminary study, both presented irregularities in the region of interest.

2. Materials and Methods

In this work, different data sources are used to carry out a comprehensive study of the selected geomagnetic storms. We analyse: (1) ionosonde observations from El Arenosillo (Spain), Roquetes (Spain), Gibilmanna (Italy) and Athens (Greece); (2) GNSS-derived TEC from receivers in the Iberian Peninsula and Western North Africa; and (3) the vertical TEC global ionosphere maps (GIMs) produced at 15 min intervals by the Universitat Politecnica de Catalunya (Spain) (UQRG, UPC Quarter-of-an-hour time resolution Rapid GIM, [20]).

2.1. Geomagnetic Storms

We study two geomagnetic storms that occurred on 26–27 February 2014 and 17–18 September 2021. Both geomagnetic storms are characterized by following a Coronal Mass Ejection (CME) from the Sun. A general view of the Space Weather and Interplanetary Magnetic Field (IMF) conditions, together with geomagnetic activity, given by geomagnetic indices, can be found in Figure 1 for both geomagnetic storms.
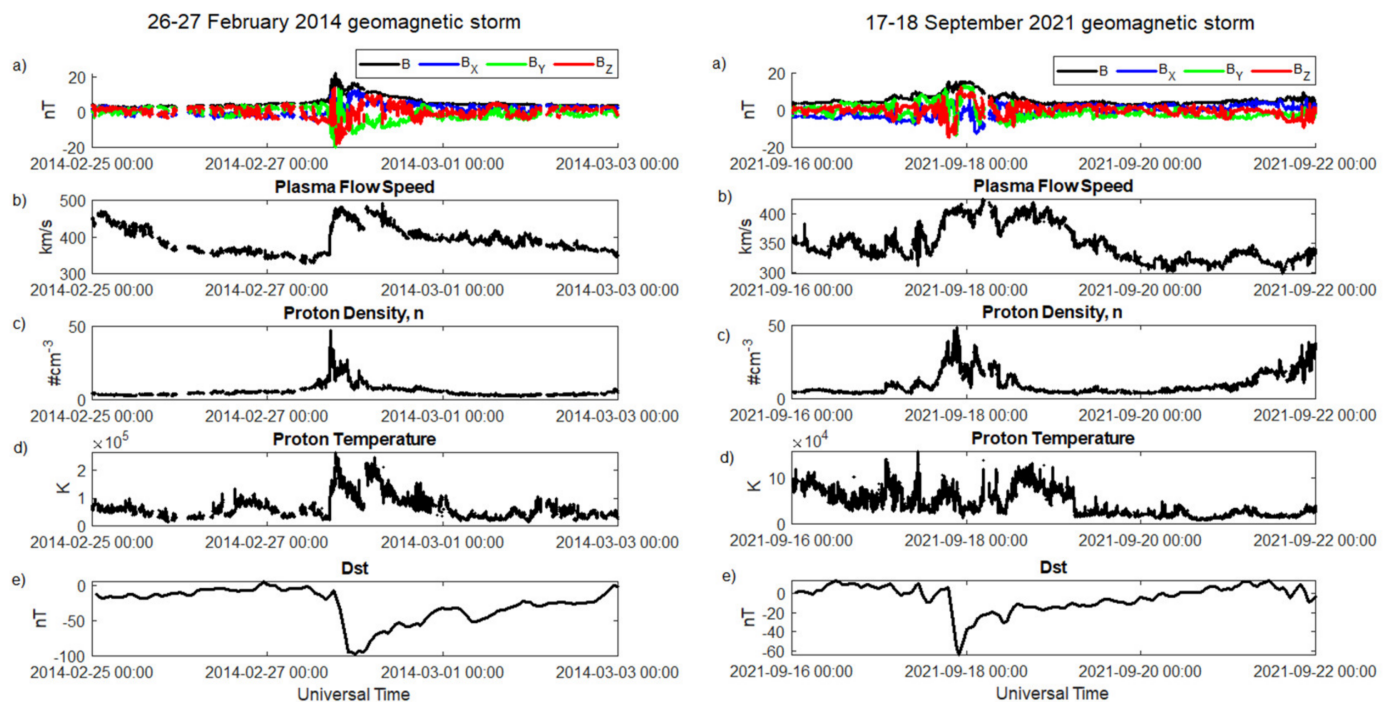
Figure 1. The Space Weather, Interplanetary Magnetic Field parameters and geomagnetic activity during (left) 25 February–2 March 2014 and (right) 16–21 September 2021: (**a**) Interplanetary Magnetic Field components and strength; (**b**) solar wind speed; (**c**) solar wind proton density and (**d**) temperature; (**e**) Dst index. Data source: OMNIWeb Data Explorer (NASA) and World Data Center for Geomagnetism (Kyoto).

In the first case study, the G2-class 26–27 February 2014 storm, the CME came from a sunspot AR1967 on 26 February. On 27 February, the maximum southward component of the IMF, at around 21 UT (12 nT, Figure 1a, left panels), and an enhancement in the solar wind speed (483 km/s, Figure 1b, left panels) were observed. This reconnected with Earth's magnetic field and developed the main phase of a geomagnetic storm on the same day. The storm continued through 28 February and quiet-time ionosphere conditions were recovered on 1 March [21]. The minimum Dst index during this geomagnetic storm was obtained on 28 February 2014 at 00 UT, with a value of -97 nT (Figure 1e, left panel).

The second case study, the 17–18 September 2021 geomagnetic storm, was classified as a minor G1-class. It started as Earth passed through the wake of a CME that hit Earth's magnetic field on 17 September at ~02 UT. The impact was very weak (Figure 1, right panels), with a detected increase of 40 km/s in the solar wind speed. The geomagnetic activity increased hours later when Earth encountered magnetic fields in the CME's wake [22]. The minimum value of the Dst index registered during this geomagnetic storm was -64 nT at 22 UT on 17 September 2021 (Figure 1e, right panel).

2.2. Ionosonde Data

From digital ionosondes, we analysed the presence of spread-F conditions, detected directly from the ionograms by visual inspection. Ionograms are studied every hour during the main phase of the storm. The Digital Ionogram DataBase (DIDbase) web portal from Global Ionospheric Radio Observatory (GIRO) and electronic Space Weather upper atmosphere (eSWua) web portal from Istituto Nazionale di Geofisica e Vulcanologia (INGV) were used to download the ionograms to detect the spread-F.

In order to reach a complete view of the ionosphere effects over the Iberian Peninsula, with special attention paid to its southern sector, we extended this analysis of the digisonde data from south to north and from west to east of the European sector, focusing especially on the Iberian Peninsula and western Africa. To do this we used data coming from El

Arenosillo (37.1 N, 6.7 W), Roquetes (40.8 N, 0.5 E), Gibilmanna (37.9 N, 14.0 E) and Athens (38.0 N, 23.5 E), as previously mentioned. The distribution of these ionosondes can be found in Figure 2.
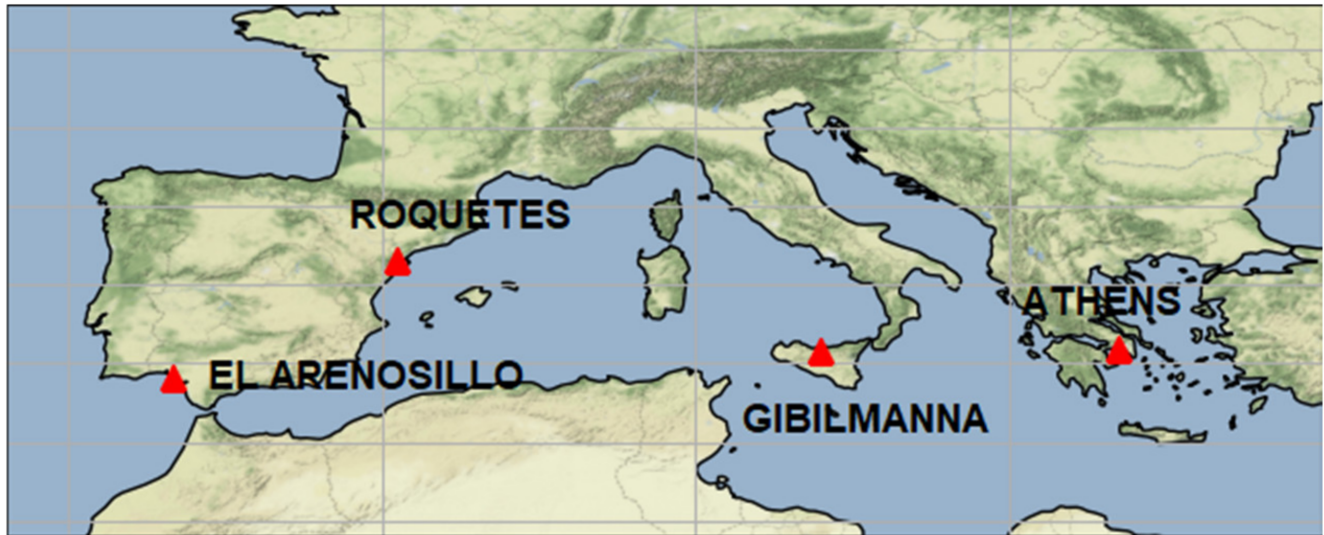

Figure 2. Map with the distribution of digital ionosondes used in this work: El Arenosillo (37.1 N, 6.7 W), Roquetes (40.8 N, 0.5 E), Gibilmanna (37.9 N, 14.0 E) and Athens (38.0 N, 23.5 E).

2.3. TEC Data

Total Electron Content (TEC) can be defined as the integral of the electron density along a path between two points, usually a GNSS receiver on the Earth's surface and a satellite. The TEC was obtained from the RINEX (Receiver Independent Exchange format) files given by the GNSS stations located in the Iberian Peninsula and in Western North Africa, coming from International GPS System (IGS), EUREF Permanent GNSS Network (EUREF), Instituto Geográfico Nacional (IGN) and other regional networks. The data were obtained every 30 s. The RINEX files were processed using a methodology given by Ciraolo et al. [23] to obtain the sTEC (slant TEC) values, with an elevation mask of 30°. Then, the ROT (Rate Of change of TEC) was calculated every 30 s, as follows:

$$ROT_i = \frac{sTEC_{i+1} - sTEC_i}{t_{i+1} - t_i} \tag{1}$$

The ROTI was calculated every 5 min as the standard deviation of the ROT. Next, an hourly average of ROTI was determined, considering all the satellites used to obtain the sTEC in order to avoid spurious effects due to the geometry or the elevation of the satellite considered.

2.4. GIMs

Global Ionosphere Maps (GIMs) of the vertical TEC are maps produced with the TEC values derived from dual frequency measurements in grids with a spacing of 5° (longitude) × 2.5° (latitude) every 2 h [24]. In this study, we used UQRG GIMs, a rapid product provided by Universitat Politècnica de Catalunya (UPC) at a higher resolution (15 min) [20]. The UQRG maps can be downloaded from https://cddis.nasa.gov/archive/gnss/products/ionex (accessed on 23 November 2022).

3. Results

3.1. Ionosonde Results

Figures 3 and 4 show, respectively, for each storm, the ionograms every 1 h during the main phase of the storms for El Arenosillo, Roquetes, Athens and Gibilmanna.
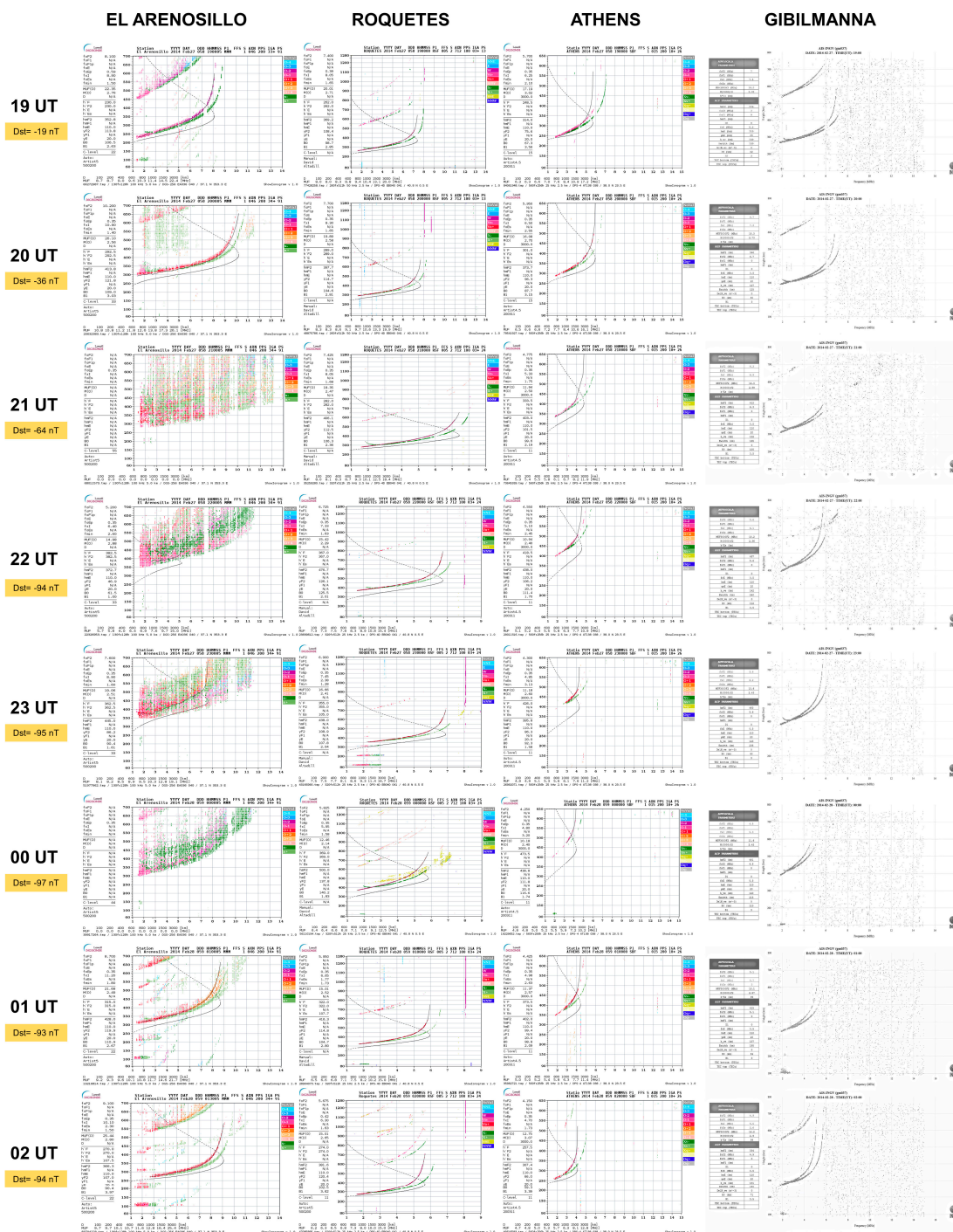
Figure 3. Ionograms (height in km vs. frequency in MHz) every 1 h from different ionosondes: El Arenosillo (first column), Roquetes (second column), Athens (third column) and Gibilmanna (fourth column), during the main phase of the 26–27 February 2014 geomagnetic storm. Legends on the left side indicate the automatically scaled parameters of the ionograms. In El Arenosillo, Roquetes and Athens ionograms, information about MUF (Maximum Usable Frequency) for oblique propagation to a corresponding range is provided in the bottom part. Colours indicate directions of the ionospheric returns and Doppler shift of overhead ordinary and extraordinary ionospheric returns. In the top part, information about the ionosonde and the date and time of the ionogram can be found in the four columns for each ionogram. Although in this work the scaled parameters of the ionograms are not analysed, we have preferred to maintain this information because ionograms are directly provided by the DIDbase web portal from GIRO and the eSWua web portal from INGV.
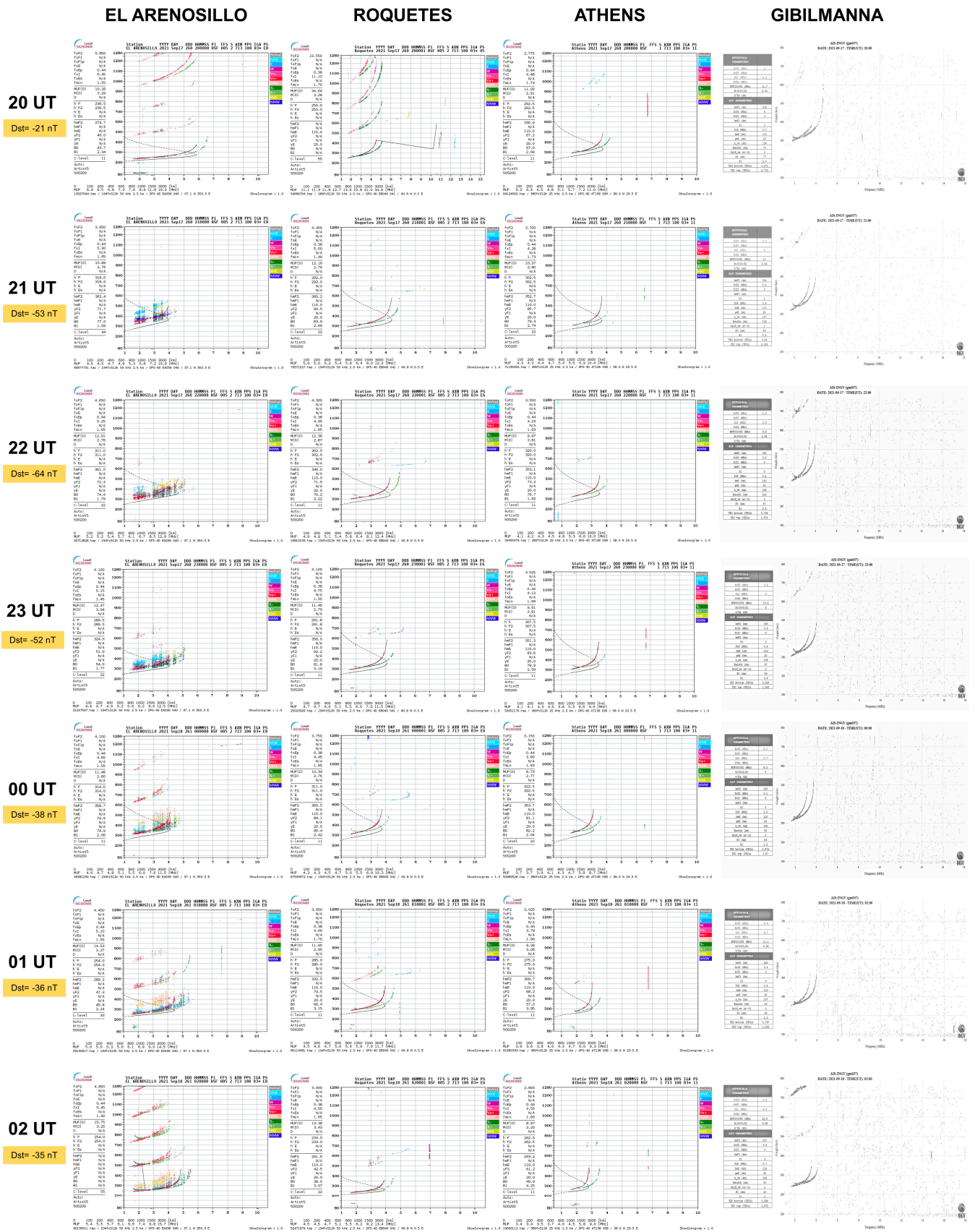
EL ARENOSILLO   **ROQUETES**   **ATHENS**   **GIBILMANNA**

Figure 4. *Cont.*

Figure 4. Ionograms (height in km vs. frequency in MHz) every 1 h from different ionosondes: El Arenosillo (first column), Roquetes (second column), Athens (third column) and Gibilmanna (fourth column), during the main phase of the 17–18 September 2021 geomagnetic storm. Legends on the left side indicate the automatically scaled parameters of the ionograms. In El Arenosillo, Roquetes and Athens ionograms, information about MUF for oblique propagation to a corresponding range is provided in the bottom part. Colours indicate directions of the ionospheric returns and Doppler shift of overhead ordinary and extraordinary ionospheric returns. In the top part, information about the ionosonde and the date and time of the ionogram can be found in the four columns for each ionogram. Although in this work the scaled parameters of the ionograms are not analysed, we have preferred to maintain this information because ionograms are directly provided by the DIDbase web portal from GIRO and the eSWua web portal from INGV.

By analysing the ionograms in Figures 3 and 4, we observed the signature of irregularities that occurred at night in the European sector local time as the spread-F in Southern Spain (El Arenosillo). Such a phenomenon was not observed at higher latitudes (Roquetes) and at eastern longitudes (Gibilmanna and Athens).

For the 26–27 February 2014 geomagnetic storm (Figure 3), El Arenosillo ionograms show spread-F from 20 UT of February 27 to 00 UT of February 28, which is particularly strong between 21 and 23 UT. Ionograms from Roquetes, Gibilmanna and Athens show no evidence of spread-F. This indicates that the presence of this phenomenon appears to be localized in the southern area of the Iberian Peninsula and at a well-defined UT.

For the 17–18 September 2021 geomagnetic storm (Figure 4), spread-F is observed in El Arenosillo ionograms from 21 UT of September 17 to 05 UT of September 18. Even though the spread-F is not particularly strong in this case, it is observed that this phenomenon takes place in El Arenosillo but not in Roquetes, Gibilmanna and Athens, and it lasts longer.

To sum up, during these two moderate storms, spread-F was observed only over the most southwestern station, located at El Arenosillo.

3.2. TEC Results and ROTI

ROTI values are calculated from the TEC measurements from north to south and from west to east in the Iberian Peninsula and in Western North Africa, and then an hourly average of ROTI is estimated.

Figures 5 and 6 show that the hourly averaged ROTI is larger in the southern region of the Peninsula and minimal in the northern region in both geomagnetic storms during the main phase, being more evident in the 2014 storm. In Figure 5, larger values of hourly averaged ROTI are also found in the west region, in comparison to eastern locations. This is not so well observed in Figure 6 for the 17–18 September 2021 geomagnetic storm, where some problems are also detected in the CASC receiver station, with no data from 08 UT.

As we mentioned before, Figures 5 and 6 show that the hourly averaged ROTI is larger in the western part of the Iberian Peninsula. This is most notable in Figure 5. In Figure 6, the hourly averaged ROTI is larger in the west than the east in north latitudes, but in the south of the Iberian Peninsula, this difference is not so evident, being equally large in all the stations. Minimal values are detected in the northeast region of the Peninsula during the main phase of both geomagnetic storms.

The location of El Arenosillo and the times of spread-F (Figures 3 and 4) correspond roughly to the times and geographical region of the occurrence of larger values of hourly averaged ROTI, as shown in Figures 5 and 6. Neither the hourly averaged ROTI of the Roquetes collocated station (EBRE), nor the receiver station near to Athens (DYNG) (see Figure S1 in the Supplementary Material), show evidence of the presence of the relevant ionosphere irregularities. This indicates that the irregularities revealed in the south and western region of the Iberian Peninsula by spread-F, and the high values of hourly averaged ROTI, appear to be a localized phenomenon in a geographical area over Europe and at a well-defined UT, because both geomagnetic storms occur in the night-time.

3.3. GIMs

Results from GIMs provide clear differences between the ionosphere behaviour before and during both geomagnetic storms (Figures 7 and 8).

Before the 26–27 February 2014 geomagnetic storm (Figure 7a,b), i.e., during quiet geomagnetic conditions, GIMs show a northern crest of the Equatorial Ionosphere Anomaly (EIA) located in Western North Africa, with low gradients and values of TEC. During the main period of the 26–27 February 2014 geomagnetic storm (Figure 7c,d), this northern crest of the EIA is located in Western North Africa and its gradients affect the southern part of the Iberian Peninsula (Figure 7c,d). Strong horizontal gradients are present both in latitude and longitude. We observe these steep gradients exclusively over this region with regard to Europe. Malki et al. [25] found the presence of a large Equatorial Plasma Bubble that, at 21 UT on 27 February 2014, covered part of Western North Africa and reached Southern Spain.

However, during 17 September 2021 (Figure 8), including the geomagnetic storm main phase (Figure 8c,d), no evidence of the presence of the equatorial anomaly is seen by the

GIMs, and gradients in the TEC are generally lacking. Notice that this last storm occurred during a period of low solar activity and it was less intense than the former.
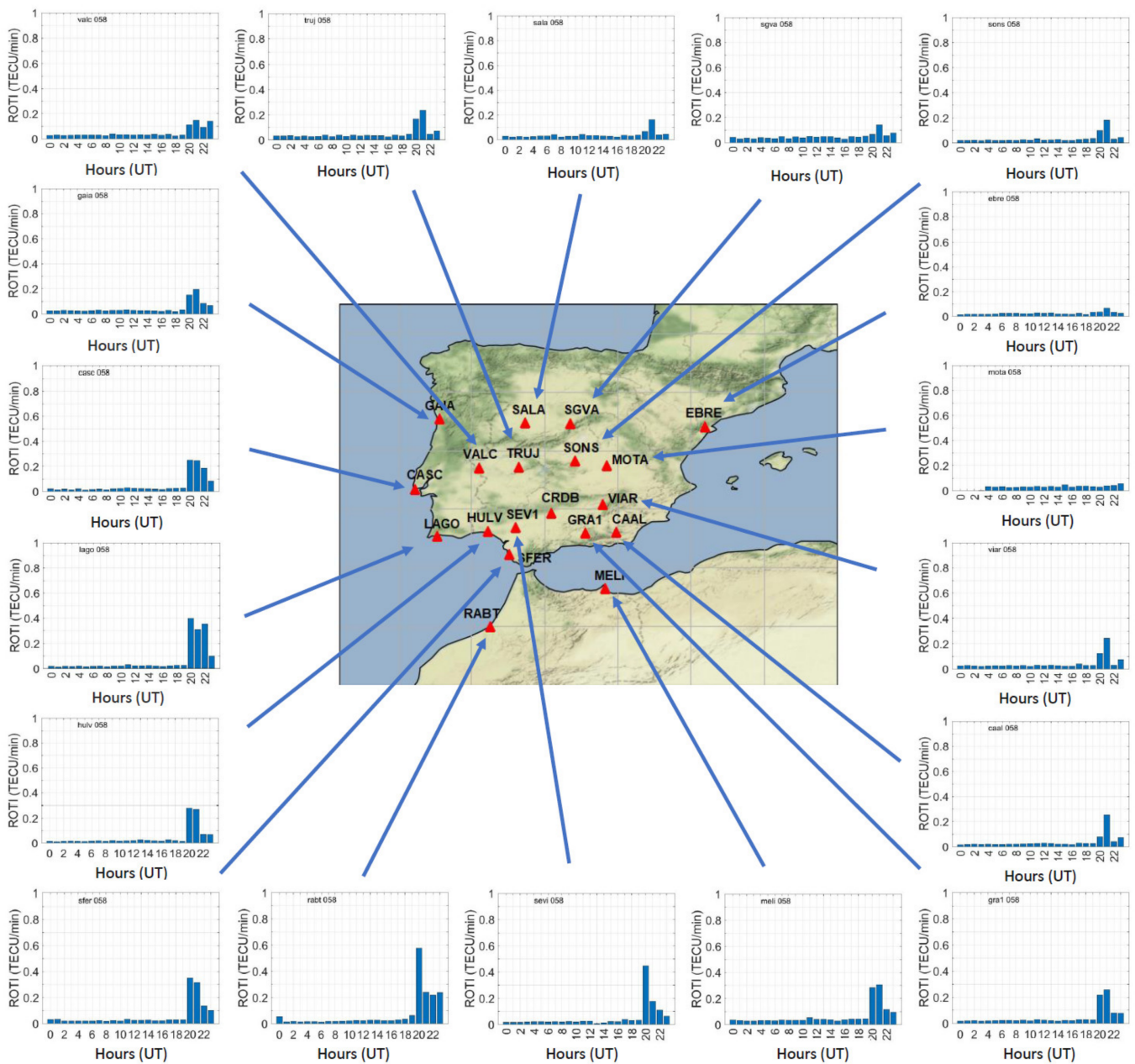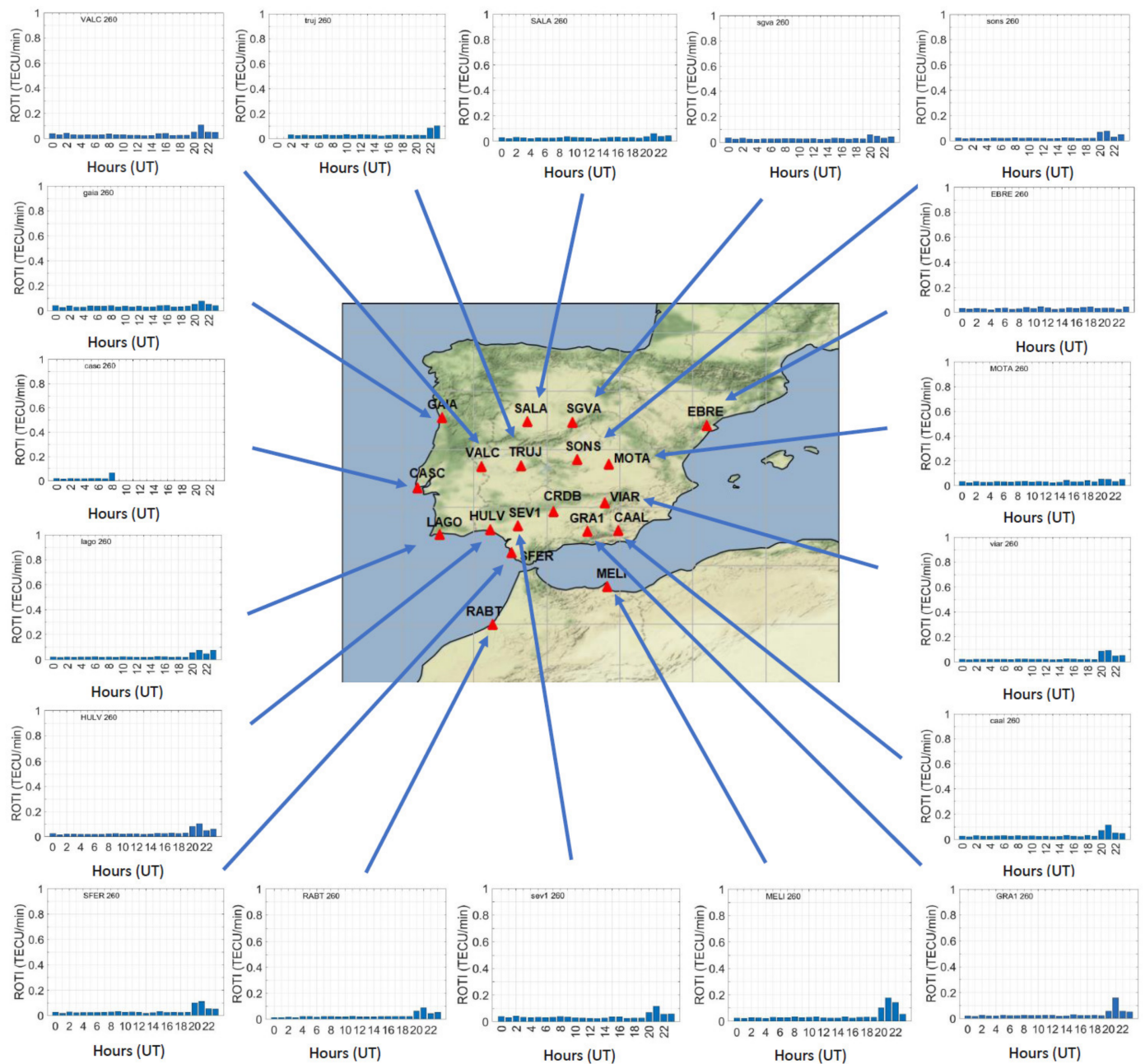

Figure 5. Map of GNSS receiver stations and hourly averaged ROTI plots during the day of the main phase of the 26–27 February 2014 geomagnetic storm (24 h on 27 February 2014): GAIA (41.1 N, 8.6 W), SALA (41.0 N, 5.7 W), SGVA (40.9 N, 4.1 W), EBRE (40.8 N, 0.5 E), VALC (39.4 N, 7.2 W), TRUJ (39.5 N, 5.9 W), SONS (39.7 N, 4.0 W), MOTA (39.5 N, 2.9 W), CASC (38.7 N, 9.4 W), LAGO (37.1 N, 8.7 W), HULV (37.3 N, 6.9 W), SEV1 (37.4 N, 6.0 W), CRDB (37.9 N, 4.8 W), VIAR (38.2 N, 3.0 W), SFER (36.5 N, 6.2 W), GRA1 (37.2 N, 3.6 W), CAAL (37.2 N, 2.5 W), RABT (34.0 N, 6.9 W), MELI (35.3 N, 2.9 W).

Figure 6. Map of receiver stations and hourly averaged ROTI plots during the day of the main phase of the 17–18 September 2021 geomagnetic storm (24 h on 17 September 2021): GAIA (41.1 N, 8.6 W), SALA (41.0 N, 5.7 W), SGVA (40.9 N, 4.1 W), EBRE (40.8 N, 0.5 E), VALC (39.4 N, 7.2 W), TRUJ (39.5 N, 5.9 W), SONS (39.7 N, 4.0 W), MOTA (39.5 N, 2.9 W), CASC (38.7 N, 9.4 W), LAGO (37.1 N, 8.7 W), HULV (37.3 N, 6.9 W), SEV1 (37.4 N, 6.0 W), CRDB (37.9 N, 4.8 W), VIAR (38.2 N, 3.0 W), SFER (36.5 N, 6.2 W), GRA1 (37.2 N, 3.6 W), CAAL (37.2 N, 2.5 W), RABT (34.0 N, 6.9 W), MELI (35.3 N, 2.9 W).
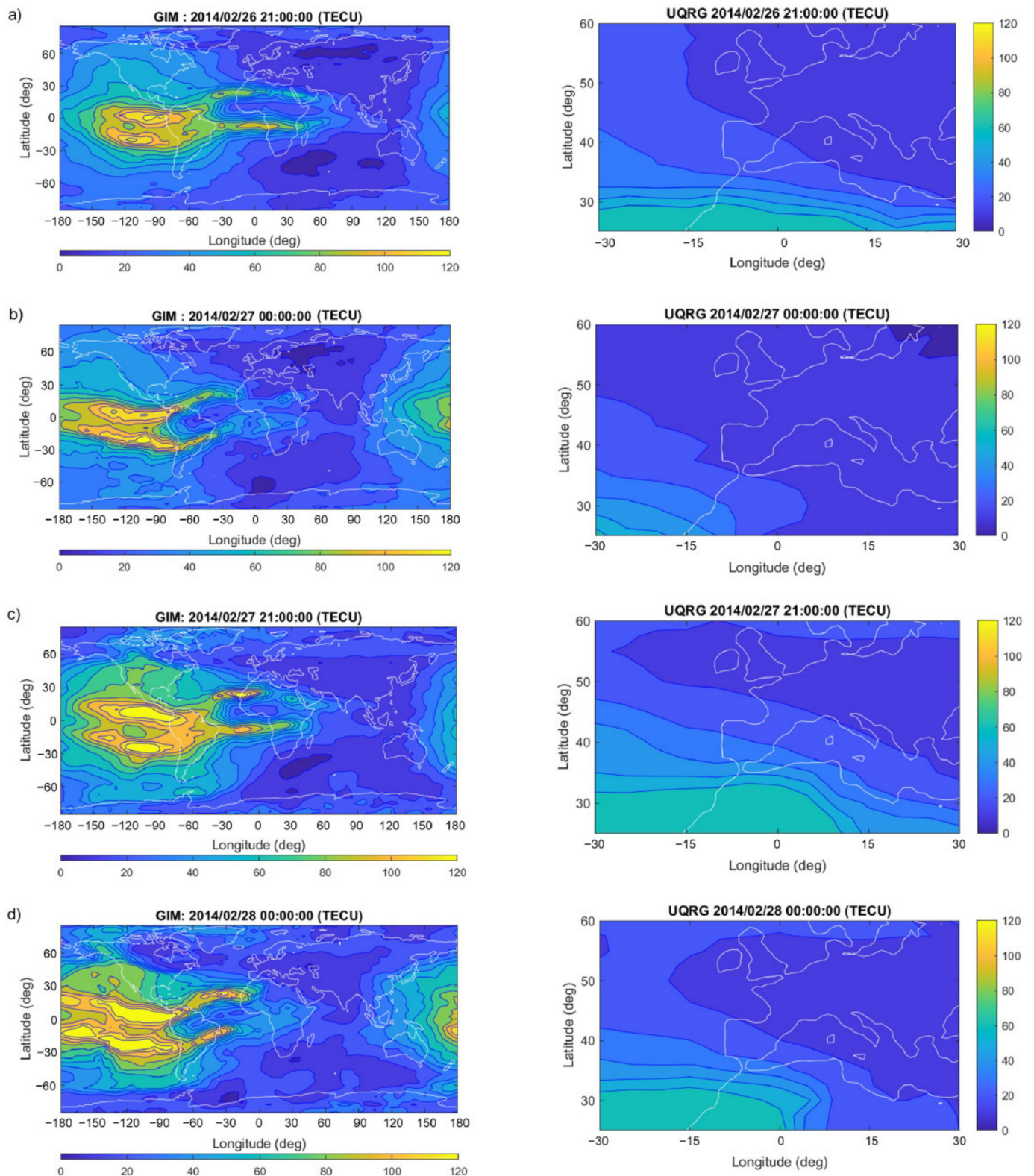
Figure 7. GIMs obtained in (**a**,**b**) quiet conditions previous to the geomagnetic storm and (**c**,**d**) in the hours of most disturbed geomagnetic conditions during the main phase (21–00 UT) of the 26–27 February 2014 geomagnetic storm. Colours indicate the values of vTEC in TECU. On the right panels, a zoom of the region of interest (Iberian Peninsula and Western North Africa) is shown.
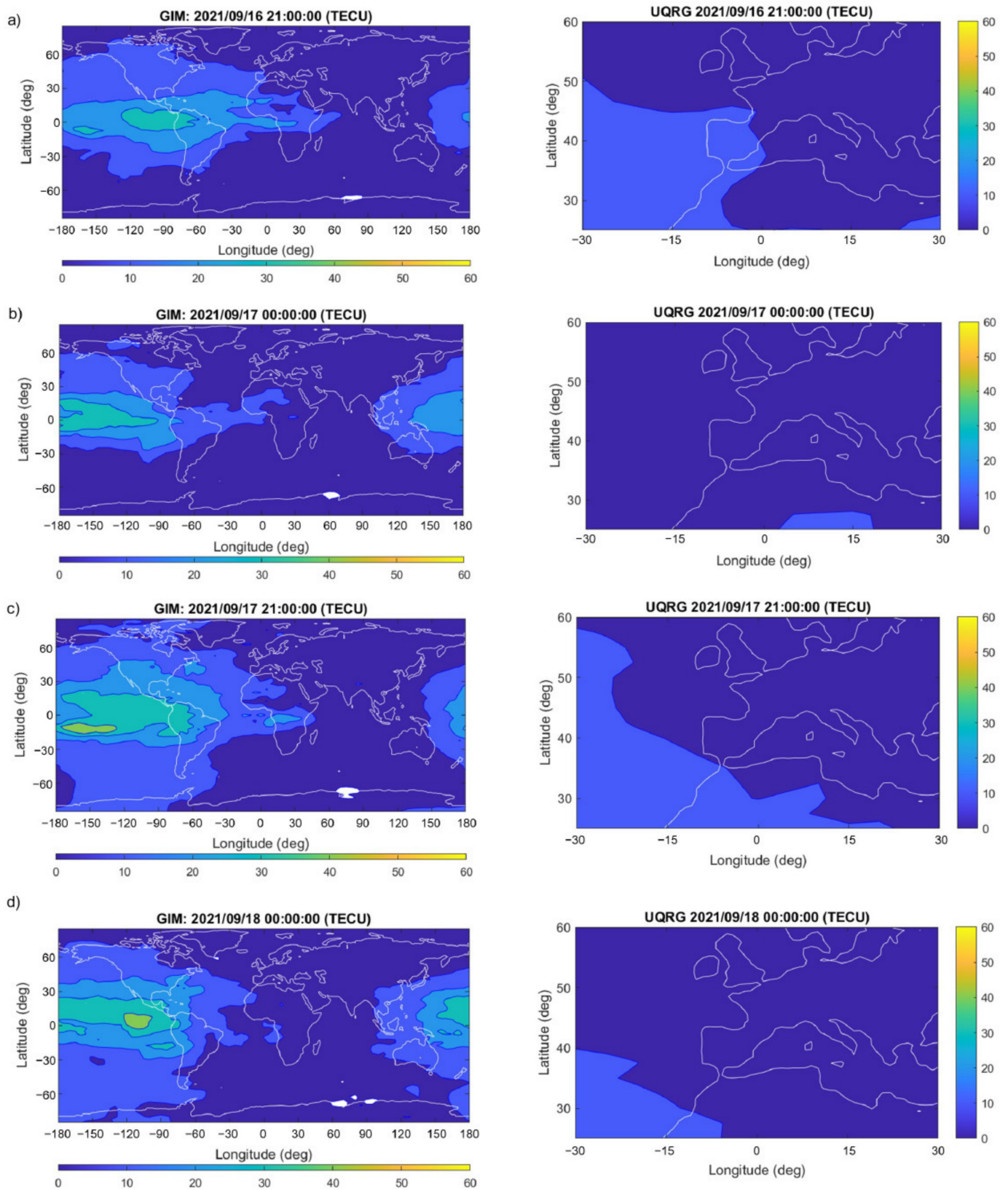
Figure 8. GIMs obtained in (**a**,**b**) quiet conditions previous to the geomagnetic storm and (**c**,**d**) in the hours of most disturbed geomagnetic conditions during the main phase (21–00 UT) of the 17–18 September 2021 geomagnetic storm. Colours indicate the values of vTEC in TECU. On the right panels, a zoom of the region of interest (Iberian Peninsula and Western North Africa) is shown.

4. Discussion

The results obtained are in agreement with the observations of Cherniak and Zakharenkova [17], and also with those of Abe et al. [10]. These authors indicated the presence of irregularities during the night-time geomagnetic storms using the ROTI data from the GNSS receiver stations, located at low geomagnetic latitudes in western Africa, and the absence of such phenomena in east African stations. It is well known that the presence of irregularities appears to be more relevant at low geomagnetic latitudes during geomagnetic storms occurring at local time night [26–28]. However, the observation of the European middle latitudes spread-F signature irregularities, localized in longitude, as seen in the present work, is worthy to be studied in depth. Although spread-F is due to small-scale irregularities (tens of meters) and ROTI is a sensing structure used on scales of a kilometre and greater, and it is not certain that the two will always occur together, as found by Sripathi et al. [29], they are both markers of instability in the ionosphere plasma.

The analysis of the ionograms and GIMs provides information about the origin of the physical phenomenon observed. The ionograms of El Arenosillo (Figures 3 and 4), a station located at both geographic and geomagnetic middle latitudes, show strong-range spread-F during the main phase of the geomagnetic storms. In the case of the 2014 storm, spread-F characteristics are similar to those commonly associated with a low latitude range spread-F, particularly in association with scintillations (see [30]). It is worth noting that scintillations are associated with an increase in the ROTI, as found in the present research (Figures 5 and 6). The ionograms that correspond to the storm of 2021 show a typical middle latitude frequency or a mixed range-frequency spread-F [3,31] of longer duration than during the 2014 storm.

At equatorial latitudes, the irregularities that give rise to strong-range spread-F, and often to scintillations of satellite signals or an increase in ROTI up to low latitudes, originate in the bottom side F layer; this is mainly through the Rayleigh–Taylor instability mechanism, as suggested originally by Dungey [32]. The occurrence of strong-range spread-F with the presence of an important increase in ROTI at a middle latitude during the 2014 storm, as shown in El Arenosillo, suggests that it should be related to a northern extension of the EIA during the main phase of the storm. Such an extension with large latitudinal gradients of the TEC in Western North Africa, including Southern Spain, appears evident in the GIMs, as shown in Figure 7. This result shows the importance of El Arenosillo digisonde for the study of this particular effect coming from low latitudes.

The occurrence of a night-time middle latitude spread-F, like those observed during the storm of 2021, can be attributed to the Perkins instabilities [33]. The presence of middle latitude frequency and mixed range-frequency spread-F during the moderate storm of August 2018 was analysed by Cherniak and Zakharenkova [34]. They found an atypical frequency and mixed frequency range spread-F condition at a middle latitude in the American coast, similar to the one reported in this paper at the time of the main phase of the 2021 storm, but with a shorter duration. These authors used other types of observations and inferred that the origin of a spread-F signature such as this could be attributed to the streamed-plasma density irregularities, observed from low latitudes toward middle latitudes. A similar process could be the cause of the spread-F signature observed in the ionograms of El Arenosillo during the 2021 storm, which were accompanied by the presence of a barely pronounced increase in the ROTI in the region. However, our knowledge of the instability mechanisms that generate these irregularities is limited, and our suggestion is only an attempt to explain it in the case of the 2021 storm, based on previous studies [34] that have observed some similar features.

5. Conclusions

To our best knowledge, this work presents the first simultaneous use of spread-F, ROTI and GIMs to analyse the presence of ionosphere irregularities during moderate geomagnetic storms over Southern Europe.

Ionosphere irregularities are present only over the southern part of the Iberian Peninsula and Western North Africa. No irregularities, as revealed by spread-F occurrence, appear eastwards of the Iberian Peninsula in Southern Europe. The results reported here are in line with the longitudinal differences in ionosphere irregularities over Africa, as reported by Azzouzi et al. [19] and Abe et al. [10], among others.

Irregularities observed during the storm of 2014, a year of high solar activity, appear to be linked to the apparent limited longitude northward extension of the EIA during the main phase of the storm, as shown by the GIMs. The observation of the EIA expansion is important because it is very localized in longitude and its effects were very localized to a region. This could be relevant to putting effort into monitoring this area during storm phenomena, in order to better understand the particular effects that seem to more extensively impact the area where we observed irregularities.

Irregularities seen during the storm of 2021, a year of low solar activity, could be linked to irregularities flowing from low to middle latitudes in a discrete longitude sector, as shown by Cherniak and Zakharenkova [34] for the North American sector.

Middle latitude irregularities during the two moderate geomagnetic storms analysed here seem to have different origin. However, an extension of the study of the occurrence of ionosphere spread-F signature irregularities at middle latitudes, during geomagnetic storms of different intensities and local times in the ionosphere monitoring location, is needed.

Conflicts of Interest: The authors declare no conflict of interest. The funders had no role in the design of the study; in the collection, analyses, or interpretation of data; in the writing of the manuscript; or in the decision to publish the results.

References

1. Aarons, J. The longitudinal morphology of equatorial F-layer irregularities relevant to their occurrence. *Space Sci. Rev.* **1993**, *63*, 209–243. [CrossRef]
2. Booker, H.G.; Wells, H.W. Scattering of radio waves by the F-region of the ionosphere. *J. Geophys. Res.* **1938**, *43*, 249–256. [CrossRef]
3. Lan, T.; Jiang, C.; Yang, G.; Sun, F.; Xu, Z.; Liu, Z. Latitudinal Differences in Spread F Characteristics at Asian Longitude Sector during the Descending Phase of the 24th Solar Cycle. *Universe* **2022**, *8*, 485. [CrossRef]
4. Alfonsi, L.; Spogli, L.; Pezzopane, M.; Romano, V.; Zuccheretti, E.; De Franceschi, G.; Cabrera, M.A.; Ezquer, R.G. Comparative analysis of spread-F signature and GPS scintillation occurrences at Tucumán, Argentina. *J. Geophys. Res. Space Phys.* **2013**, *118*, 4483–4502. [CrossRef]
5. Woodman, R.F.; La Hoz, C. Radar observations of F region equatorial irregularities. *J. Geophys. Res.* **1976**, *81*, 5447–5466. [CrossRef]
6. Weber, E.J.; Buchau, J.; Eather, R.H.; Mende, S.B. North-south aligned equatorial airglow depletions. *J. Geophys. Res. Space Phys.* **1978**, *83*, 712–716. [CrossRef]
7. Booker, H.G. Turbulence in the ionosphere with applications to meteor-trails, radio-star scintillation, auroral radar echoes, and other phenomena. *J. Geophys. Res.* **1956**, *61*, 673–705. [CrossRef]
8. Aarons, J.; Mendillo, M.; Yantosca, R.; Kudeki, E. GPS phase fluctuations in the equatorial region during the MISETA 1994 campaign. *J. Geophys. Res. Space Phys.* **1996**, *101*, 26851–26862. [CrossRef]
9. Pi, X.; Mannucci, A.J.; Lindqwister, U.J.; Ho, C.M. Monitoring of global ionospheric irregularities using the worldwide GPS network. *Geophys. Res. Lett.* **1997**, *24*, 2283–2286. [CrossRef]
10. Abe, O.E.; Rabiu, A.B.; Radicella, S.M. Longitudinal Asymmetry of the Occurrence of the Plasma Irregularities over African Low-Latitude Region. *Pure Appl. Geophys.* **2018**, *175*, 4355–4370. [CrossRef]
11. Thanh, D.N.; Le Huy, M.; Amory-Mazaudier, C.; Fleury, R.; Saito, S.; Chien, T.N.; Thi Thu, H.P.; Le Truong, T.; Thi, M.N. Characterization of ionospheric irregularities over Vietnam and adjacent region for the 2008-2018 period. *Vietnam. J. Earth Sci.* **2021**, *43*, 1–20. [CrossRef]
12. Balan, N.; Liu, L.; Le, H. A brief review of equatorial ionization anomaly and ionospheric irregularities. *EPP* **2018**, *2*, 257–275. [CrossRef]
13. Migoya-Orué, Y.O.; Radicella, S.M.; Coïsson, P. Low latitude ionospheric effects of major geomagnetic storms observed using TOPEX TEC data. *Ann. Geophys.* **2009**, *27*, 3133–3139. [CrossRef]
14. Abdu, M.A. Major phenomena of the equatorial ionosphere thermosphere system under disturbed conditions. *J. Atmos. Solar Terr. Phys.* **1997**, *59*, 1505–1519. [CrossRef]
15. Tanaka, T. Low-latitude ionospheric disturbances: Results for March 22, 1979, and their general characteristics. *Geophys. Res. Lett.* **1986**, *13*, 1399–1402. [CrossRef]
16. Lin, C.H.; Richmond, A.D.; Heelis, R.A.; Bailey, G.J.; Lu, G.; Liu, J.Y.; Yeh, H.C.; Su, S.-Y. Theoretical study of the low- and midlatitude ionospheric electron density enhancement during the October 2003 superstorm: Relative importance of the neutral wind and the electric field. *J. Geophys. Res.* **2005**, *110*, A12312. [CrossRef]
17. Cherniak, I.; Zakharenkova, I. First observations of super plasma bubbles in Europe. *Geophys. Res. Lett.* **2016**, *43*, 137–145. [CrossRef]
18. Kashcheyev, A.; Migoya-Orué, Y.; Amory-Mazaudier, C.; Fleury, R.; Nava, B.; Alazo-Cuartas, K.; Radicella, S.M. Multivariable comprehensive analysis of two great geomagnetic storms of 2015. *J. Geophys. Res. Space Phys.* **2018**, *123*, 5000–5018. [CrossRef]
19. Azzouzi, I.; Migoya-Orue, Y.; Amory Mazaudier, C.; Fleury, R.; Radicella, S.M.; Touzani, A. Signatures of solar event at middle and low latitudes in the Europe-African sector, during geomagnetic storms, October 2013. *Adv. Space Res.* **2015**, *56*, 2040–2055. [CrossRef]
20. Orús, R.; Hernández-Pajares, M.; Juan, J.; Sanz, J. Improvement of global ionospheric VTEC maps by using kriging interpolation technique. *J. Atmos. Sol.-Terr. Phys.* **2005**, *67*, 1598–1609. [CrossRef]
21. Sur, D.; Hammou Ali, O.; Binti Sarudin, I.; Rupiewicz, J.; Bravo, M.; Toriashvili, L.; Sun, X. Effects of Geomagnetic Storm on Equatorial Ionization during 27 February–1 March, 2014. In Proceedings of the AGU Fall Meeting 2018, Washington, DC, USA, 10–14 December 2018.
22. SpaceWeather.com. Available online: https://www.spaceweather.com/archive.php?view=1&day=17&month=09&year=2021 (accessed on 11 October 2022).
23. Ciraolo, L.; Azpilicueta, F.; Brunini, C.; Meza, A.; Radicella, S.M. Calibration errors on experimental slant total electron content (TEC) determined with GPS. *J. Geod.* **2007**, *81*, 111–120. [CrossRef]
24. Hernández-Pajares, M.; Juan, J.M.; Sanz, J.; Orus, R.; Garcia-Rigo, A.; Feltens, J.; Komjathy, A.; Schaer, S.C.; Krankowski, A. The IGS VTEC maps: A reliable source of ionospheric information since 1998. *J. Geod.* **2009**, *83*, 263–275. [CrossRef]

25.   Malki, K.; Bounhir, A.; Benkhaldoun, Z.; Makela, J.J.; Vilmer, N.; Fisher, D.J.; Kaab, M.; Elbouyahyaoui, K.; Harding, B.J.; Laghriyeb, A.; et al. Ionospheric and thermospheric response to the 27–28 February 2014 geomagnetic storm over north Africa. *Ann. Geophys.* **2018**, *36*, 987–998. [CrossRef]

26.   Basu, S.; Kelly, M.C. Review of equatorial scintillation phenomena in light of recent developments in the theory and measurement of equatorial irregularities. *J. Atmos. Terr. Phys.* **1977**, *39*, 1229–1247. [CrossRef]

27.   Fejer, B.G.; Scherliess, L.; de Paula, E.R. Effects of the vertical plasma drift velocity on the generation and evolution of equatorial spread F. *J. Geophys. Res.* **1999**, *104*, 19859–19869. [CrossRef]

28.   Magdaleno, S.; Herraiz, M.; Altadill, D.; de la Morena, B.A. Climatology characterization of equatorial plasma bubbles using GPS data. *J. Space Weather Space Clim.* **2017**, *7*, A3. [CrossRef]

29.   Sripathi, S.; Sreekumar, S.; Banola, S. Characteristics of equatorial and low-latitude plasma irregularities as investigated using a meridional chain of radio experiments over India. *J. Geophys. Res. Space Phys.* **2018**, *123*, 4364–4380. [CrossRef]

30.   Shi, J.K.; Wang, G.J.; Reinisch, B.W.; Shang, S.P.; Wang, X.; Zherebotsov, G.; Potekhin, A. Relationship between strong range spread F and ionospheric scintillations observed in Hainan from 2003 to 2007. *J. Geophys. Res.* **2011**, *116*, A08306. [CrossRef]

31.   Paul, K.S.; Haralambous, H.; Oikonomou, C.; Paul, A.; Belehaki, A.; Ioanna, T.; Kouba, D.; Buresova, D. Multi-station investigation of spread F over Europe during low to high solar activity. *J. Space Weather Space Clim.* **2018**, *8*, A27. [CrossRef]

32.   Dungey, J.W. Convective diffusion in the equatorial F region. *J. Atmos. Terr. Phys.* **1956**, *9*, 304–310. [CrossRef]

33.   Perkins, F. Spread F and ionospheric currents. *J. Geophys. Res.* **1973**, *78*, 218–226. [CrossRef]

34.   Cherniak, I.; Zakharenkova, I. Development of the storm-induced ionospheric irregularities at equatorial and middle latitudes during the 25–26 August 2018 major geomagnetic storm. *Space Weather* **2022**, *20*, e2021SW002891. [CrossRef]